Supplementary Figures: Azimuthal seismic anisotropy in the Earth's upper mantle and the thickness of tectonic plates

A.J. Schaeffer[1], S. Lebedev[2] and T.W. Becker[3]

Geophysical Journal International

July 2016

1. University of Ottawa
2. Dublin Institute for Advanced Studies
3. University of Texas at Austin

Table S1: Level of significance between the radially averaged correlation coefficients contained in Table 1 for the depth range 50–700 km, computed following the method of Becker et al. (2007). The upper half of the table is for $\langle r_8 \rangle$ and the lower half is for $\langle r_{20} \rangle$.

	SL2016svA-YB13sv	SL2016svAr-YB13sv	SL2016svA-DR2012a	SL2016svAr-DR2012a	SL2016svA-3D2015-07Sva	SL2016svAr-3D2015-07Sva	YB13sv-DR2012a	YB13sv-3D2015-07svA
SL2016svA-YB13sv		0.00	0.059	0.284	0.060	0.230	0.434	0.386
SL2016svAr-YB13sv	0.139		0.059	0.284	0.060	0.230	0.434	0.386
SL2016svA-DR2012a	0.314	0.181		0.228	0.119	0.173	0.382	0.333
SL2016svAr-DR2012a	0.434	0.309	0.134		0.340	0.057	0.166	0.112
SL2016SvA-3D2015-07Sva	0.139	0.000	0.181	0.309		0.288	0.484	0.438
SL2016SvAr-3D2015-07Sva	0.395	0.268	0.090	0.045	0.268		0.221	0.168
YB13sv-DR2012a	0.635	0.534	0.383	0.260	0.534	0.302		0.055
YB13sv-3D2015-07Sva	0.574	0.465	0.304	0.175	0.465	0.219	0.087	

Table S2: Level of significance between the radially averaged correlation coefficients contained in Table 1 for the depth range 50–300 km, computed following the method of Becker et al. (2007). The upper half of the table is for $\langle r_8 \rangle$ and the lower half is for $\langle r_{20} \rangle$.

	SL2016svA-YB13sv	SL2016svAr-YB13sv	SL2016svA-DR2012a	SL2016svAr-DR2012a	SL2016svA-3D2015-07Sva	SL2016svAr-3D2015-07Sva	YB13sv-DR2012a	YB13sv-3D2015-07svA
SL2016svA-YB13sv		0.145	0.467	0.038	0.580	0.114	0.528	0.528
SL2016svAr-YB13sv	0.503		0.580	0.184	0.677	0.256	0.408	0.408
SL2016svA-DR2012a	0.058	0.548		0.436	0.144	0.369	0.821	0.821
SL2016svAr-DR2012a	0.222	0.309	0.277		0.552	0.077	0.556	0.556
SL2016SvA-3D2015-07Sva	0.349	0.742	0.296	0.537		0.492	0.873	0.873
SL2016SvAr-3D2015-07Sva	0.057	0.456	0.115	0.166	0.400		0.612	0.612
YB13sv-DR2012a	0.824	0.499	0.846	0.716	0.929	0.800		0.000
YB13sv-3D2015-07Sva	0.804	0.461	0.828	0.689	0.919	0.778	0.047	

Table S3: Level of significance between the radially averaged correlation coefficients contained in Table 1 for the depth range 300–700 km, computed following the method of Becker et al. (2007). The upper half of the table is for $\langle r_8 \rangle$ and the lower half is for $\langle r_{20} \rangle$.

	SL2016svA-YB13sv	SL2016svAr-YB13sv	SL2016svA-DR2012a	SL2016svAr-DR2012a	SL2016svA-3D2015-07Sva	SL2016svAr-3D2015-07Sva	YB13sv-DR2012a	YB13sv-3D2015-07svA
SL2016svA-YB13sv		0.083	0.318	0.460	0.190	0.391	0.391	0.293
SL2016svAr-YB13sv	0.088		0.393	0.527	0.270	0.462	0.462	0.369
SL2016svA-DR2012a	0.483	0.552		0.160	0.135	0.081	0.081	0.027
SL2016svAr-DR2012a	0.550	0.613	0.085		0.290	0.081	0.081	0.187
SL2016SvA-3D2015-07Sva	0.336	0.414	0.170	0.252		0.213	0.213	0.108
SL2016SvAr-3D2015-07Sva	0.517	0.583	0.043	0.043	0.211		0.000	0.107
YB13sv-DR2012a	0.517	0.583	0.043	0.043	0.211	0.000		0.107
YB13sv-3D2015-07Sva	0.412	0.485	0.085	0.170	0.086	0.128	0.128	

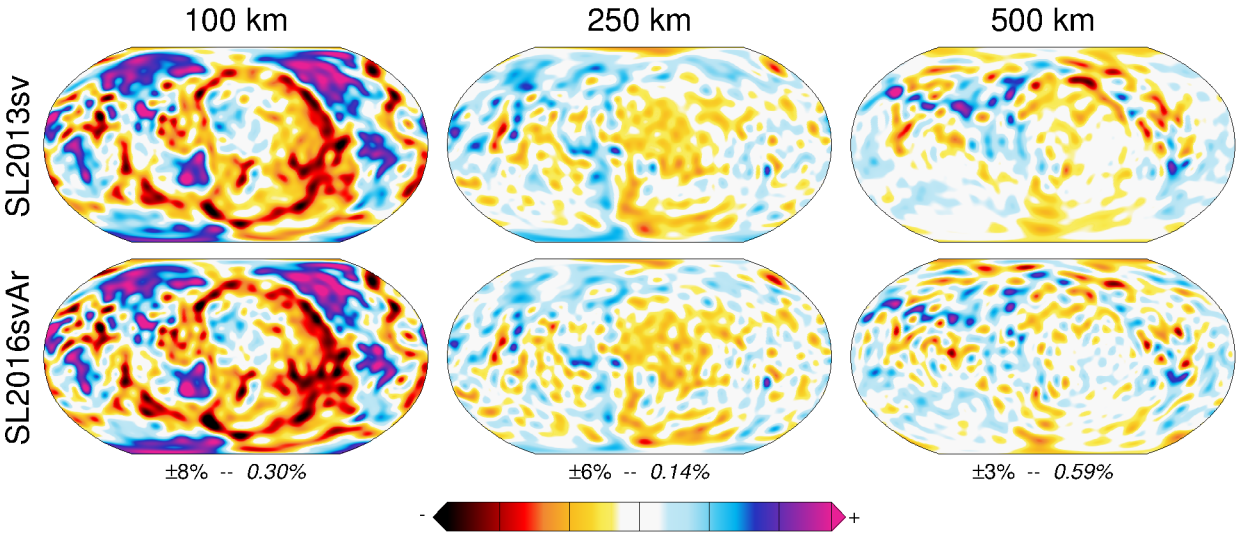

Figure S1: Comparison of isotropic component of SL2016svA (top row, SL2013sv; Schaeffer & Lebedev (2013)) with the isotropic component of SL2016svAr (bottom row) at depths of 100, 250 and 500 km. Below each pair of panels, the saturation limits in percent are indicated, followed by the difference in RMS perturbations between each set of panels.

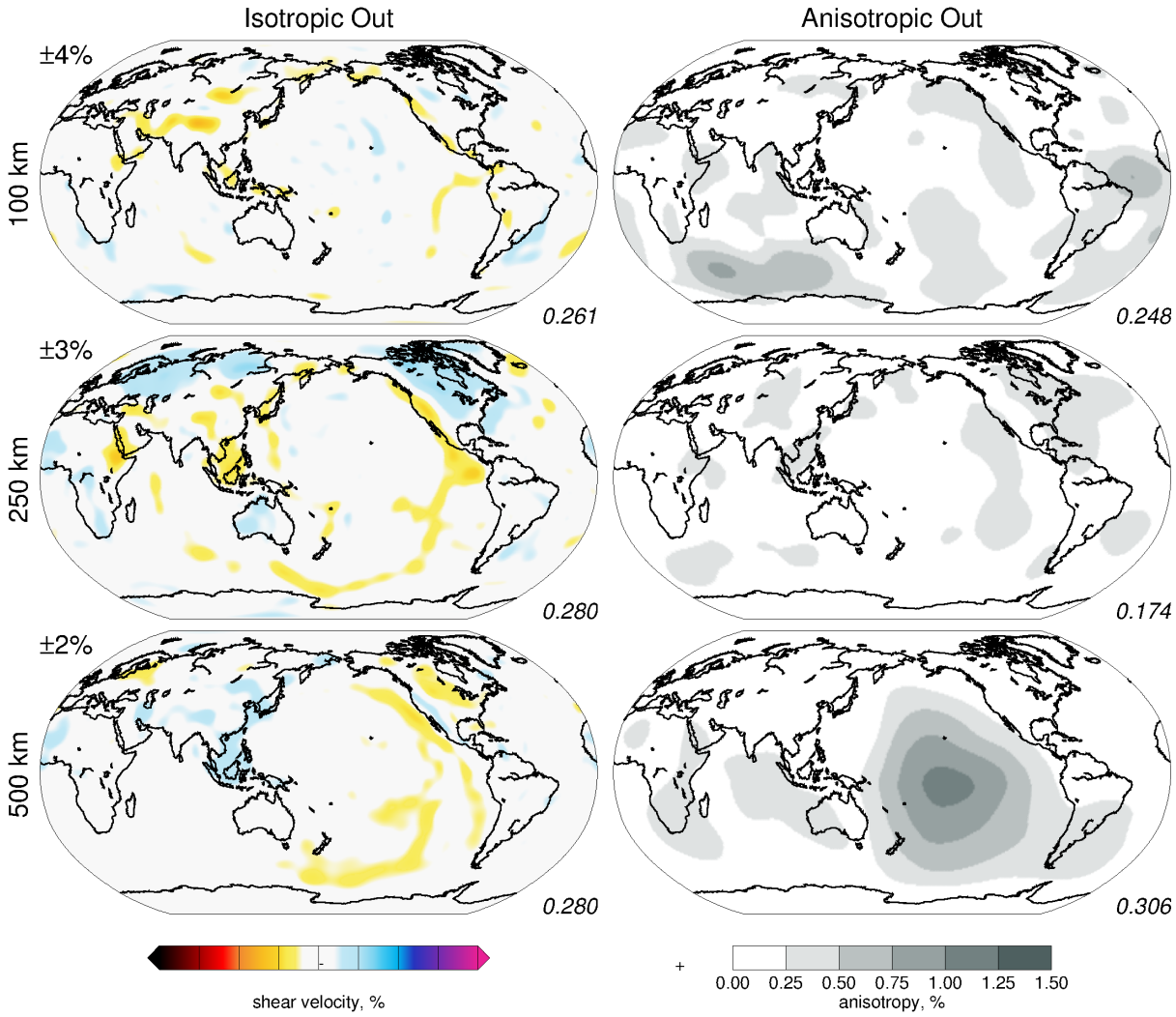

Figure S2: Synthetic tests illustrating the leakage between the isotropic and anisotropic model parameters. The results of two tests are illustrated at depths of 100, 250 and 500 km. The left panels illustrate the isotropic velocity anomalies that result from the inversion of a synthetic dataset generated from a purely anisotropic model, whereas the right panels show the anisotropic structure resulting from the inversion of a synthetic dataset derived from an isotropic model. Colour scales are indicated beneath each set of panels. Saturation limits for isotropic velocity are denoted top left of each map. For both isotropic and anisotropic maps, the RMS perturbation in percent is denoted at bottom right.

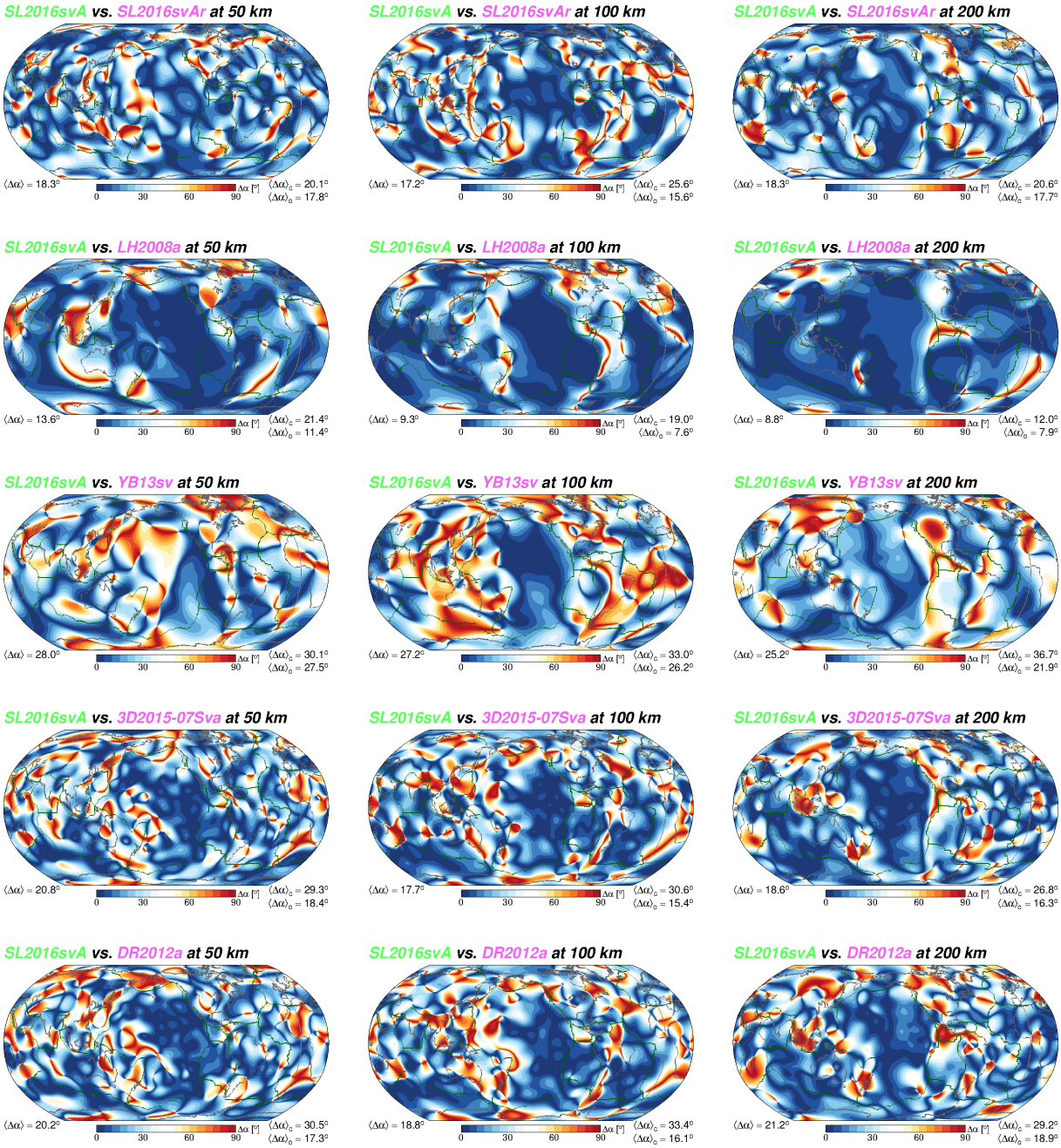

Figure S3: Angular misfit of SL2016svA compared with five other azimuthal anisotropy models: SL2016svAr, LH2008a (Lebedev & van der Hilst, 2008; Becker et al., 2012), YB13sv (Yuan & Beghein, 2013), 3D2015-07Sva (Debayle et al., 2016) and DR2012a (Debayle & Ricard, 2013), at depths of 50 km (left column), 100 km (centre column), and 200 km (right column). The colour scale indicates misfit in azimuthal anisotropy orientation between the models, with weighting based on the amplitude on SL2016svA. Global average angular misfit ($\langle\Delta\alpha\rangle$) is indicated at the lower left of each panel, with the continental ($\langle\Delta\alpha\rangle_c$) and oceanic ($\langle\Delta\alpha\rangle_o$) averages at lower right.

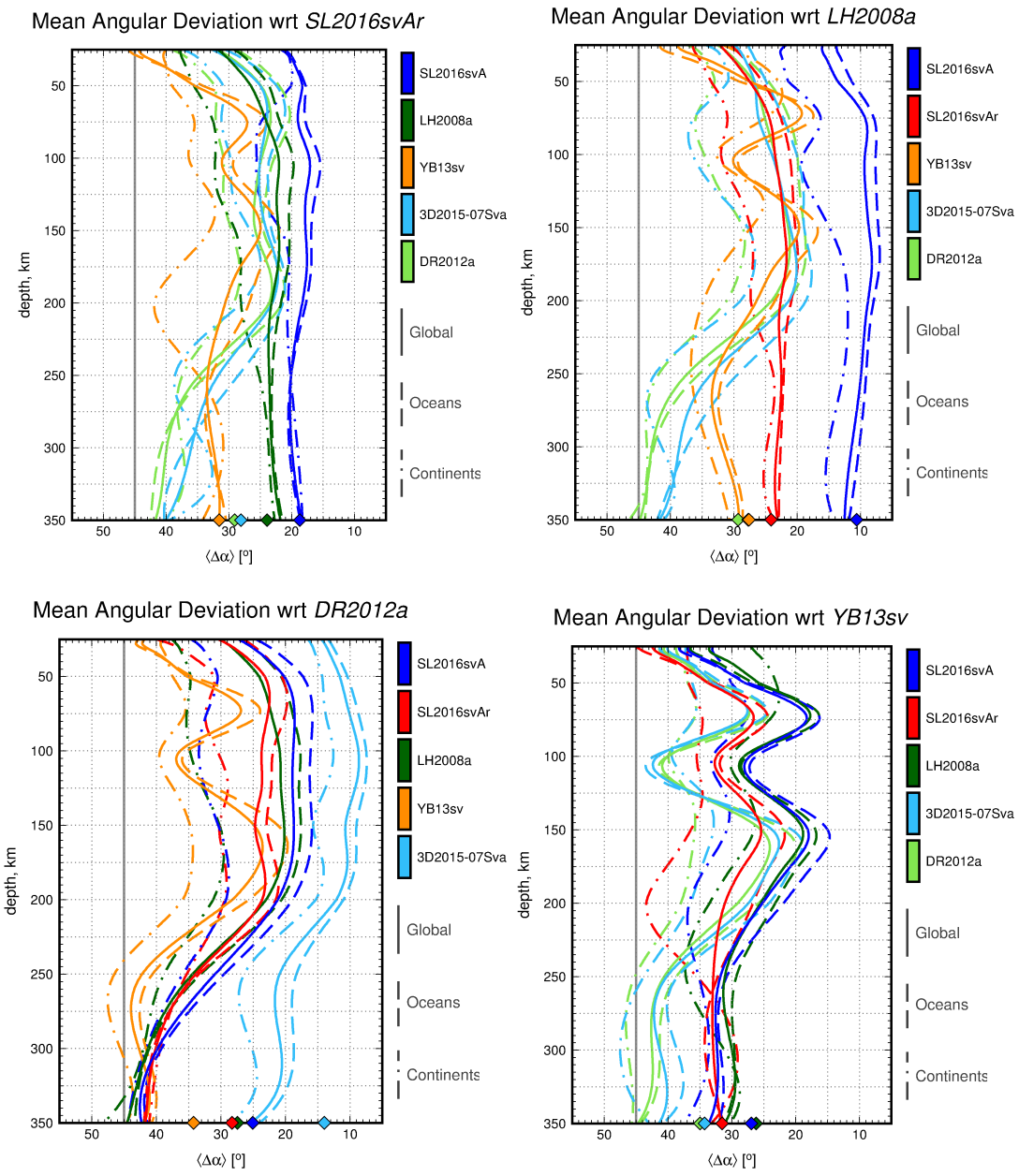

Figure S4: Average angular misfit $\langle \Delta\alpha \rangle$ of fast-propagation directions in seismic anisotropy models as a function of depth, with respect to SL2016svAr, LH2008a (Lebedev & van der Hilst, 2008; Becker et al., 2012), DR2012a (Debayle & Ricard, 2013), 3D2015-07Sva (Debayle et al., 2016) and YB13sv (Yuan & Beghein, 2013). Solid curves: the global averages; dashed: for oceanic regions only; dash-dotted: continental regions only. Filled diamonds along the bottom axis indicate the depth-averaged global misfit for each model. Light grey line at $\langle \Delta\alpha \rangle = 45°$ indicates a random average orientation between the two models. Note that the colours representing the different models change between the different panels.

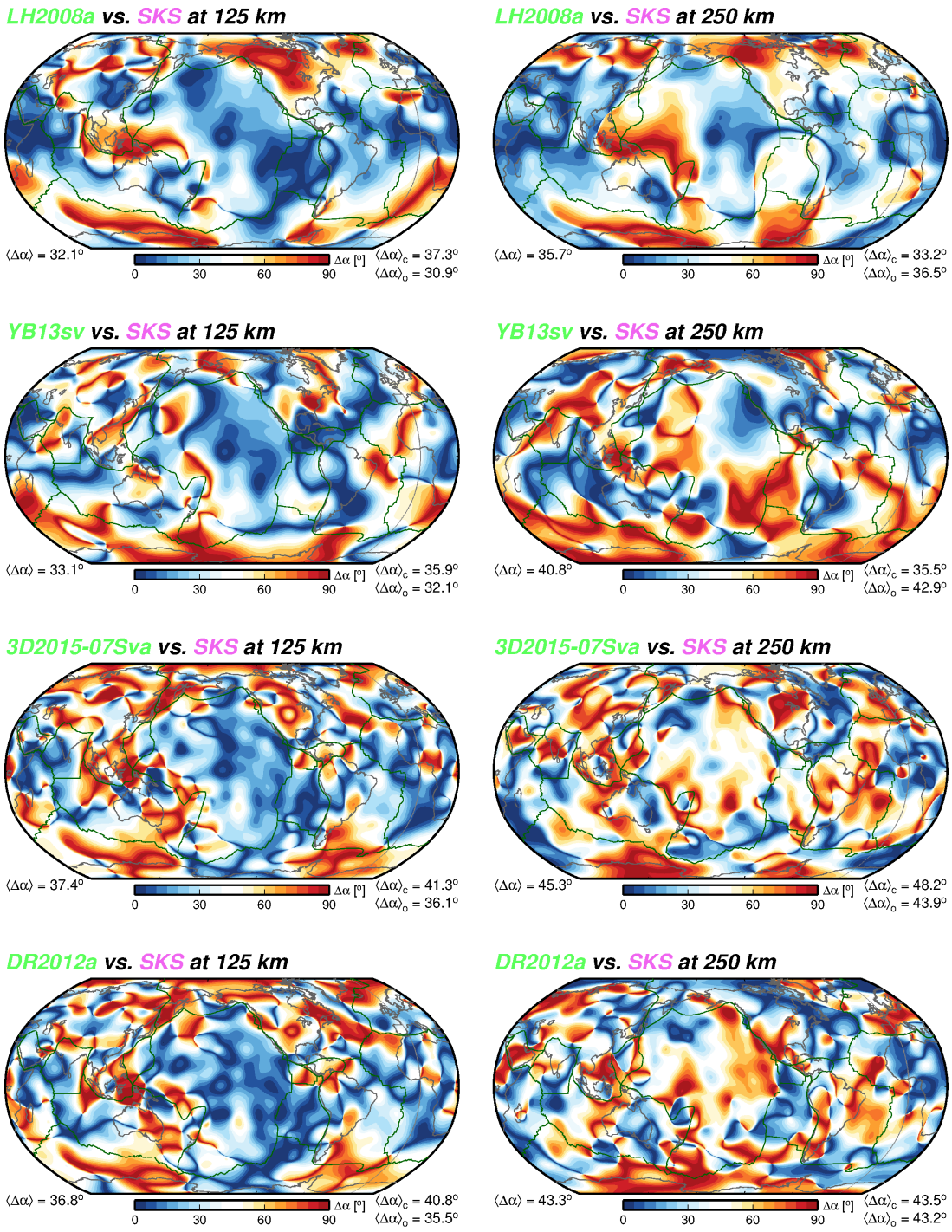

Figure S5: Angular misfits between fast-propagation directions in tomographic models LH2008a (Lebedev & van der Hilst, 2008; Becker et al., 2012), YB13sv (Yuan & Beghein, 2013), 3D2015-07Sva (Debayle et al., 2016) and DR2012a (Debayle & Ricard, 2013) with the global spherical harmonic expansion of SKS splitting distribution from Becker et al. (2012), for depths of 125 km (left column) and 250 km (right column). For both the tomographic models and SKS splitting, anisotropy was expanded in generalized spherical harmonics up to maximum angular degree 20. The colour scale indicates misfit in azimuthal anisotropy orientation between the models, with weighting based on the amplitude of the tomography model. Global average angular misfit ($\langle\Delta\alpha\rangle$) is indicated at the lower left of each panel, with the continental ($\langle\Delta\alpha\rangle_c$) and oceanic ($\langle\Delta\alpha\rangle_o$) averages at the lower right.

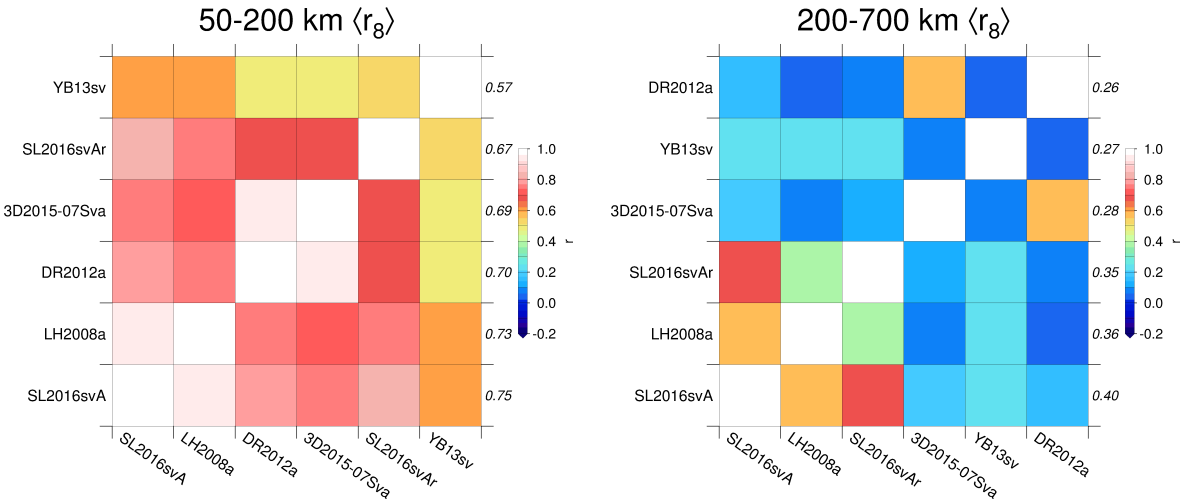

Figure S6: Comparison of radially averaged inter-model correlations for global, upper-mantle anisotropy models, up to and including degree 8 ($\langle r_8 \rangle$). The left panel illustrates correlations for the upper mantle at 50-200 km depths; the right panel shows the correlations for the depth range 200-700 km. In each panel, the models are sorted (left-right, bottom-up) by the decreasing total correlation (excluding auto-correlation, the white squares along the diagonal); these values are shown along the right vertical axis of each panel. Note that the sorting of the models differs between the two depth ranges.

References

Becker, T. W., Ekström, G., Boschi, L., & Woodhouse, J. H., 2007. Length scales patterns, and origin of azimuthal seismic anisotropy in the upper mantle as mapped by Rayleigh waves, *Geophys. J. Int.*, **171**(1), 451–462.

Becker, T. W., Lebedev, S., & Long, M. D., 2012. On the relationship between azimuthal anisotropy from shear wave splitting and surface wave tomography, *J. Geophys. Res.*, **117**(B1), 1–17.

Debayle, E. & Ricard, Y., 2013. Seismic observations of large-scale deformation at the bottom of fast-moving plates, *Earth Planet. Sc. Lett.*, pp. 1–13.

Debayle, E., Kennett, B. L. N., & Priestley, K., 2005. Global azimuthal seismic anisotropy and the unique plate-motion deformation of Australia., *Nature*, **433**(7025), 509–12.

Debayle, E., Dubuffet, F., & Durand, S., 2016. An automatically updated s-wavemodel of the upper mantle and the depth extent of azimuthal anisotropy, *Geophys. Res. Lett.*, **43**, 1–8.

Lebedev, S. & van der Hilst, R. D., 2008. Global upper-mantle tomography with the automated multimode inversion of surface and S-wave forms, *Geophys. J. Int.*, **173**, 505–518.

Schaeffer, A. J. & Lebedev, S., 2013. Global shear speed structure of the upper mantle and transition zone, *Geophys. J. Int.*, **194**(1), 417–449.

Yuan, K. & Beghein, C., 2013. Seismic anisotropy changes across upper mantle phase transitions, *Earth Planet. Sc. Lett.*, **374**, 132–144.